Cellulose (2025) 32:7535–7552
https://doi.org/10.1007/s10570-025-06690-w

ORIGINAL RESEARCH

A semi-automatic workflow for atomic force microscopy image analysis and cellulose nanocrystal particle size measurements

Saba Karimi · Sezen Yucel · Robert J. Moon · Linda J. Johnston · Nathan J. Bechle · Warren Batchelor · Jae-Young Cho · Surya R. Kalidindi

Received: 27 February 2025 / Accepted: 14 July 2025 / Published online: 14 August 2025

Abstract The reliable measurement of cellulose nanocrystal (CNC) particle morphology is vital for ongoing CNC production optimization and application development. A semi-automatic image analysis program, SMART-AFM, was developed for CNC particle size measurements from atomic force microscopy (AFM) images and subsequently used to analyze the AFM images acquired from four laboratories that participated in the interlaboratory comparison (ILC) study by Bushell et al.. SMART-AFM demonstrated a 40 times faster analysis compared to the manual approach used in the ILC. A detailed image-to-image analysis showed that SMART-AFM produced similarly accurate results as compared to the manual method for CNC identification, as well as length and height measurements. SMART-AFM "correctly" identified CNCs 82–90% and manual analysis identified 83–94%, depending on the given laboratory image dataset. While SMART-AFM reported mean length values consistently 7–16.5% lower than the manual approach—attributed to trimming CNC tails during segmentation—CNC height measurements were in closer agreement—an average difference of 4.2%. Moreover, SMART-AFM CNC identification and measurement demonstrated lower variability across images from different laboratories, potentially indicating higher identification consistency compared to the subjective and qualitative nature of manual analysis. The strengths and challenges of SMART-AFM in analyzing images affected by AFM imaging artifacts is systematically studied. An analysis is presented to reaffirm the importance of measuring 300–500 CNCs to ensure a representative, reliable measurement results. Overall, SMART-AFM is established as a standardized CNC identification and measurement tool, with improved speed compared to the manual alternative, and proven consistency and reliability. The SMART-AFM code is publicly available in Github™.

Supplementary Information The online version contains supplementary material available at https://doi.org/10.1007/s10570-025-06690-w.

S. Karimi · S. R. Kalidindi
School of Materials Science and Engineering, Georgia Institute of Technology, Atlanta, GA 30332, USA

S. Yucel · S. R. Kalidindi
George W. Woodruff School of Mechanical Engineering, Georgia Institute of Technology, Atlanta, GA 30332, USA

R. J. Moon (✉) · N. J. Bechle
The Forest Products Laboratory, U.S.D.A. Forest Service, Madison, WI 53726, USA
e-mail: robert.j.moon@usda.gov

L. J. Johnston
Metrology Research Centre, National Research Council Canada, Ottawa, ON K1A 0R6, Canada

W. Batchelor
Department of Chemical and Biological Engineering, Monash University, Clayton, VIC 3800, Australia

J.-Y. Cho
Quantum and Nanotechnology Research Centre, National Research Council Canada, Edmonton, AB T6G 2M9, Canada

Graphical abstract

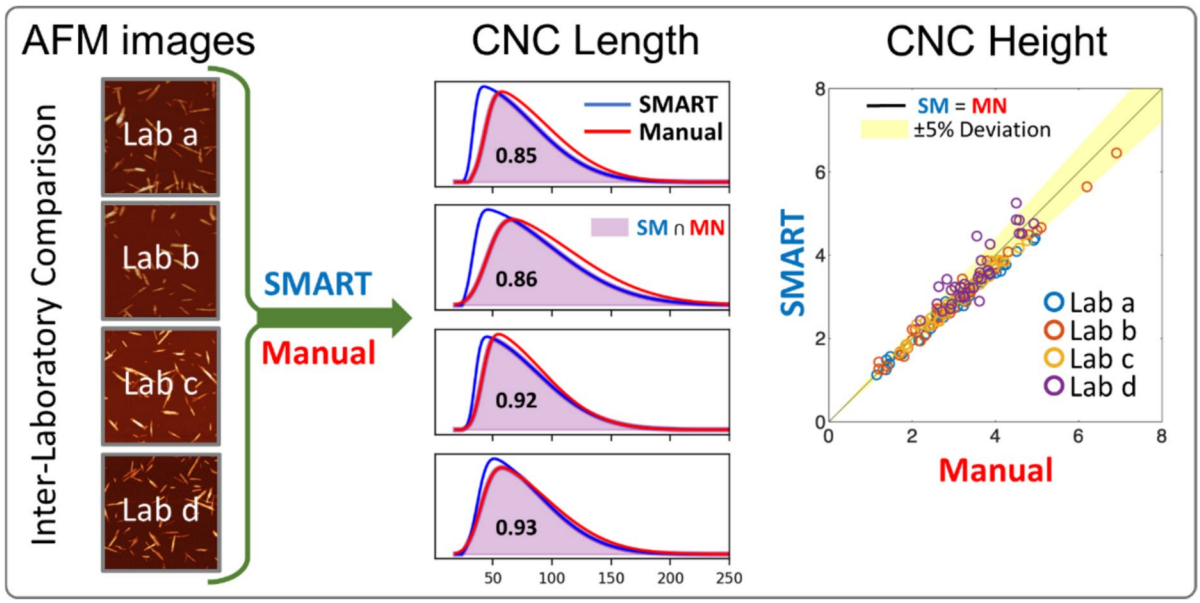

Keywords Cellulose nanocrystals · Atomic force microscopy · Interlaboratory comparison · Semi-automatic image analysis · Particle size measurements

Introduction

Cellulose nanocrystals (CNCs) are cellulose-based nanomaterials typically produced by acid hydrolysis of woody plants. They commonly exhibit a spindle-like particle morphology with diameters of 4–20 nm and lengths ranging from 50 to 500 nm, often tapering at the ends. (Foster et al. 2018; Moon et al. 2011). The term "CNC" broadly covers a variety of CNC morphologies and surface characteristics influenced by production method, reaction conditions and the starting cellulose source material (Elazzouzi-Hafraoui et al. 2009; Moon et al. 2011; Reid et al. 2017; Foster et al. 2018; Schütz et al. 2018; da Silva et al. 2020; Delepierre et al. 2021; Grachev et al. 2024). Consequently, reliable characterization of CNC particle size and size distribution is crucial for quality control, grade definitions and ensuring reproducibility in their intended applications (Schütz et al. 2018; Johnston 2024). The capability to rapidly measure large numbers of CNC particle dimensions facilitates investigation into CNC morphology effects in optimizing performance. Transmission electron microscopy (TEM) and atomic force microscopy (AFM) are widely used to measure CNC particle size (Reid et al. 2017; Jakubek et al. 2018; Meija et al. 2020; da Silva et al. 2020; Bushell et al. 2021; Delepierre et al. 2021; Grachev et al. 2024). TEM imaging provides CNC length and width information, while AFM image provides height, length and width information. However, AFM tip convolution effects artificially increase dimensions of the object being imaged; this is significant for CNC width as it can be a high fraction of the total width, while it is small for CNC length, as it is a small fraction of the total length. Thus, most AFM studies of CNC particle size measurement only report the height and length. Currently, TEM and AFM image analyses typically requires an analyst to manually perform a one-by-one selection of individual CNC followed by a repetitive procedure to measure their length and diameter. The imaging and manual image analysis protocols for CNC particle size measurement are established and are summarized in two interlaboratory comparisons (ILC) studies, Meija et al. (2020) and Bushell et al.

(2021) for TEM and AFM, respectively, and in ISO technical specification (ISO/TS 23151).

Challenges in CNC particle size measurements arise from CNC material variations, imaging limitations, and image analysis issues. Material issues include CNC particle shape variability, broad size distributions, and strong aggregation propensity. Imaging challenges stem from difficulties in preparing a well-dispersed CNC sample on the imaging substrate as well as obtaining high contrast, low noise images with minimal imaging artifacts and well-defined particle–substrate edges. While TEM images have low particle-background contrast and high noise, AFM imaging has higher contrast and lower noise, but may suffer from AFM tip inconsistencies and artifacts. Finally, image analysis is hindered by analyst subjectivity, inconsistency and fatigue, making it difficult to identify individual CNCs consistently and determine particle–substrate edges for measurements. The ILC studies by Meija et al. (2020) and Bushell et al. (2021) involving ten participating research groups showed how differences in imaging equipment, imaging settings and analyst judgement in particle selection and measurements affect CNC size analysis for a CNC reference material (CNCD-1 2016). The TEM-ILC study concluded that analyst bias and sample heterogeneity were the primary sources of variability, suggesting automated image analysis methods as a potential solution to reduce the subjectivity in choice of analyzable CNCs.

Current manual analysis approaches typically use open-source software such as ImageJ for TEM images (Mattos et al. 2019; Meija et al. 2020) and Gwyddion for AFM images (Mattos et al. 2019; Bushell et al. 2021), however, these are difficult to automate for CNCs. Open-source automated image analysis software is available for the identification and dimensional measurement (i.e., length, width, and orientation) of fibrils with high aspect ratio, including FiberApp (Usov and Mezzenga 2015; Persson et al. 2017), DiameterJ (Hotaling et al. 2015), FibrilJ (Sokolov et al. 2017), and a custom Python package developed by Willhammar et al. (2021). FiberApp has been used to analyze both CNC and cellulose nanofibrils (CNFs) and the Willhammar Python package has been utilized for images of CNFs, but not for CNCs. Similarly, the AutoDetect program (Wang et al. 2021) developed for the automated analysis of TEM images from low aspect ratio metal nanoparticles requires low noise, high contrast between particles and background and simple particle morphology—smooth edge and shapes—parameters often difficult to achieve with CNC imaging.

Challenges to deploying the available image analysis tools for CNC image analysis involve accounting for image quality characteristics (high noise, low edge contrast, overlapping particles) and the variation and inconsistency of CNC morphology. To enhance CNC selection, improve measurement consistency, and to reduce analysis time, an automated image analysis approach tailored for CNC particle identification and dimensional analysis is needed. A semi-automated image analysis framework focused on CNCs (Standardized Morphology Analysis for Research and Technology—SMART) was developed by Yucel et al. (2021) for TEM and AFM image analysis. Using datasets from TEM and AFM characterization of CNC reference material CNCD-1 (2016), which included 434 TEM and 66 AFM images, SMART image analysis was critically compared to the conventional manual approaches reported by Jakubek et al. (2018). SMART demonstrated a high overlap with the manual approach in identifying individual CNCs, over 50% for TEM and 70% for AFM and consistent CNC particle size measurement and distribution, with a much faster throughput. SMART processed images at less than 1.5 and 0.4 s per CNC in TEM and AFM images, respectively, running in MATLAB on a laptop computer (i7 3.7 GHz processor, 16GB RAM) as compared to an estimate of 30 s per CNC for manual analysis.

Yucel et al. (2022) evaluated SMART using TEM images from four different laboratories involved in the ILC study (Meija et al. 2020), focusing on CNC particle size distributions. Critical comparisons between SMART and manual analysis showed overall agreement in CNC length and width, but with substantially faster throughput and modest differences in the overall particle size distributions. Both SMART and manual approaches required the use of high-quality TEM images, characterized by low background noise, high CNC-background contrast, distinct CNC edges, and a low density of CNCs homogeneously distributed on the imaging substrate. The SMART-TEM code is publicly available on GitHub™.

In the current study, SMART was redesigned for AFM images (SMART-AFM) and applied to datasets from four of the participating laboratories in ILC

study by Bushell et al. (2021). The following aspects were explored using SMART-AFM: effects of image quality on CNC identification (e.g., background noise, contrast, imaging artifacts, CNC distribution density), image analysis approach (e.g., SMART versus manual approaches), and an assessment of representative measurements for length and height. The results obtained from the SMART-AFM approach were compared critically against the results obtained from the conventional manual approaches used within the ILC study.

Methodology

AFM sample preparation and imaging

This study uses the AFM images from the ILC study by Bushell et al. (2021), obtained from the certified CNC reference material, CNCD-1 (2016), with all samples prepared by the piloting laboratory and sent to participants for AFM imaging and analysis. A detailed protocol for imaging and CNC identification and analysis is provided in the supplementary information in Bushell et al. (2021). The protocol specified flattening the raw AFM images using a first order polynomial after excluding CNCs through threshold masking. An analysis protocol using Gwyddion (open-source software for date visualization and analysis for scanning probe microscopy data) was provided, although participants could select other software if the same criteria for selection of individual CNCs for analysis were used. The Gwyddion protocol prescribed the analyst to draw a line through the long axis of all individual CNCs and then measure the maximum height and length for each particle with respect to the local background level for each particle. AFM images from all labs have undergone some level of pre-processing (e.g., flattening) using native AFM (or Gwyddion) software prior to the Gwyddion analysis protocol. The extent of this pre-processing varied across laboratories and is not documented. Therefore, the term "as-received" refers to the initial state of the images before any additional manual or SMART processing and analysis.

Of the ten ILC study participating laboratories, four (Lab2, Lab6, Lab7, and Lab10) were selected for SMART analysis (Table 1). These four laboratories were selected for the variation in the reported mean lengths and heights and in the number of AFM probes used.

Table 1 Measurement summary from the ILC study report (Bushell et al. 2021)

	Lab2	Lab6	Lab7	Lab10
Number of images*	40	25	47	44
Number of probes	3	4	14	1
Number of CNCs	544	409	620	500
Mean L (std)**	83 (31)	99 (42)	79 (30)	82 (34)
Mean H (std)**	2.9 (0.8)	3.3 (1.3)	3.1 (1.2)	3.5 (1.2)
Mean AR (std)**	31 (12)	32 (12)	28 (9)	24 (9)

*The ILC article did not report the number of images for each laboratory. We acquired the relevant information from the as-received data

**The values for mean length (L), height (H), and height aspect ratio (AR = L/H) are for skew normal fits to the data, along with the standard deviation (std) in parentheses

SMART-AFM image analysis framework

The original SMART program reported in Yucel et al. (2021), which was later adapted for TEM images and denoted as SMART-TEM in Yucel et al. (2022), was redesigned and customized for CNC identification and measurement for AFM images and is rebranded as SMART-AFM. On a high-level, the SMART-AFM framework is summarized in Fig. 1, and includes (a) segmentation; a filter-based image processing workflow to identify CNC objects from the background, (b) classification of CNCs into four groups based on visual features, and (c) digital size measurement of CNCs. Each step includes functions with adjustable parameters that can be calibrated to suit specific CNC material or image quality, representing the semi-automatic aspect of SMART. Once these parameters are determined, SMART-AFM can process large batches of images automatically, ensuring both flexibility and efficiency. Detailed MATLAB functions and parameters are provided in Tables S1–S5 of the supplementary material. The appropriate order and magnitude of each parameter was determined through the critical analysis of a set of 5 as-received AFM images from each of the participating laboratories. For this study, SMART-AFM was empirically optimized with a single, unified parameter set for all analysis. For simplicity, SMART-AFM will be referred to as SMART throughout the remainder of the document.

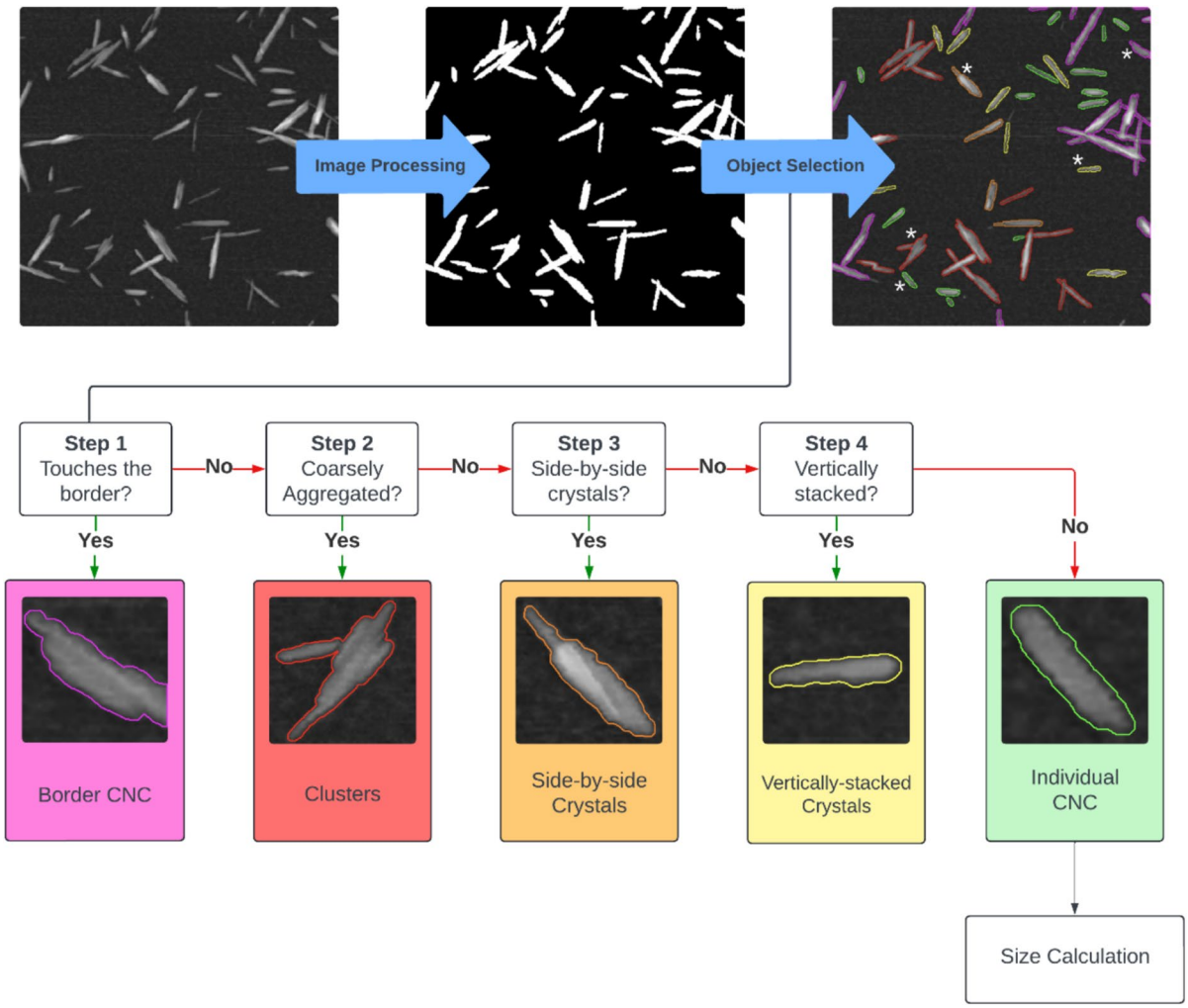

Fig. 1 Flow chart of SMART image analysis framework that starts with an as-received AFM image (top left image), which is segmented, and then analyzed by SMART to identify and categorize objects (top right image), and finally, size measurement of individual CNCs. Examples of each of the five classifications of CNC particles are given, the locations of which are shown with asterisks (*) at the top right image

Image processing

Image processing in the SMART framework includes the following steps: (a) pre-processing to correct AFM artifacts, reduce noise, enhance contrast, and increase resolution (b) segmentation to separate CNC objects from background, and (c) post-processing to address segmentation errors. In image pre-processing, a given AFM image, structured as a matrix of 512 × 512 height values (Z) in the X–Y plane, is first corrected for abnormally tall height "spikes" in the image (Fig. S1). Height values are constrained to a 15 nm range. The minimum height within the is retained and a maximum height threshold is set to 15 nm above the minimum, with any value above the threshold mapped to the height threshold. The resulting 512 × 512 matrix is linearly mapped to double precision values between 0 and 1 and then discretized to integers between 0 and 255 to yield an 8-bit grayscale image. The initial height thresholding increases the 8-bit resolution of the processed images with height outliers. Next, the resulting image is "upscaled" by a factor of 4 in the X–Y dimensions (512 × 512 to 2048 × 2048 pixels), followed by a 2D Gaussian

filter to smooth the resulting larger image. Upscaling increases the image resolution while maintaining the original spatial scale, which effectively decreases the pixel size compared to a typical CNC resulting in a smoother, more accurate representation of the physical CNC boundaries (Fig. S2). Subsequent image processing steps are contrast enhancement, background noise removal using a high-pass Fast Fourier Transform filter, sharpening, and an edge-preserving median filter for further reduction of background noise (parameters are summarized in Table S1).

For segmentation, adaptive thresholding was used to segment the pre-processed grayscale image into binary 1 and 0, separating the foreground CNC objects from the substrate background, respectively. In this method, the grayscale value of each pixel is compared to its local neighborhood of approximately 150 nm in size; pixels higher than the local average are segmented as foreground—CNC object—and those lower than local average are segmented as background. Each connected component of foreground pixels is called a "CNC object".

Post-processing removes false positives from segmentation, for example substrate pixels falsely segmented as foreground, a typical byproduct of noisy imaging (discussed in a following subsection—image quality assessment). They appear in two distinct forms: (a) small cluster of substrate pixels far from CNCs are misclassified as foreground, which is caused from the local segmentation thresholding neighborhood average only containing substrate pixels. (b) Bright substrate pixels near CNC pixels are misclassified as foreground attached to CNC objects, creating a dilated, or bumpy CNC boundary (Fig. S3). These two types require different treatments. The small, isolated substrate regions (a) are eliminating by identifying and removing objects with an area smaller than 0.02% of the upscaled image area, or those objects with a median pixel intensity less than 30. Bright substrate pixels near CNCs (b) are processed by refining particle boundaries with another local thresholding segmentation, intended to separate dark substrate pixels, bright substrate pixels, and brighter CNC pixels. The process applies two thresholds to the masked local neighborhood, defined as the bounding box of the object expanded 60% in X–Y directions, with any other present CNC objects in the neighborhood masked out. The resulting ternary image, composed of 0's, 1's and 2's, identifies connected objects. Only objects with median intensity greater than 30 in the upscaled image are retained. These steps effectively refine CNC boundaries and remove segmentation errors caused by the attachment of neighboring noisy "bright" pixels (Fig. S3).

CNC grouping identification

CNCs within an AFM image are broadly classified as either isolated or agglomerated. Isolated CNCs are well-separated from other CNCs and surrounded only by substrate pixels. Agglomerated CNCs are connected to at least one other crystal through touching, crossing, overlapping, vertical stacking or clustering (Fig. 1). Agglomerated CNCs are not deconstructed to the constituent individual crystals and are segmented as single CNC objects. The identified CNC objects are categorized into four groups: coarse clusters, laterally bundled (e.g., side-by-side touching), vertically stacked, or individual CNCs.

The segmentation and object grouping framework uses AFM data in all three dimensions (X–Y image scanning plane and the Z-height) to classify CNC objects within each image via a sequential 4 step grouping process. Each step identifies and groups non-isolated CNCs, leaving the remaining particles as isolated individual CNCs (Fig. 1). In step 1, CNC objects touching the edges of the image are grouped as "border CNCs". The remaining CNC objects are sequentially grouped via steps 2, 3, and 4 as being coarse clusters, lateral bundles, or vertical stacks of crystals, respectively, and are considered as three different groups of agglomerated CNCs. Steps 2, 3, and 4 require the application of a set of transformations to the objects for a suitable comparison against the selection criteria of that step. These transformations include rotation, dilation and erosion, hole filling in object boundaries, and convolution (Tables S3 and S4 include the functions utilized in the grouping steps).

Step 2 identifies coarse clusters, characterized by multiple crystals in contact (overlapping or lateral bundles of parallel crystals) that exceed the reported range of dimensions for a single CNC measured via AFM, while accounting for AFM tip convolution effects on measurements: long axis 10–300 nm, and short axis 10–40 nm (Bushell et al. 2021). A CNC object in SMART is classified as a coarse cluster based on its shape metrics in the X–Y plane: width

aspect ratio[1] (less than 1.9), solidity[2] (less than 85%), and major axis (outside 10–300 nm) and minor axis (outside 10–40 nm). For each CNC object, a representative bounding box, is obtained by rotating the object to align the image plane x-axis and the major axis of an ellipse sharing a normalized central moment with the CNC object (Fig. S4). The major and minor axes are defined as the long and short sides of the bounding box, respectively, with length/width aspect ratio being the ratio of major and minor axes. The solidity threshold of 85% accounts for crystal imperfections and imaging artifacts.

Step 3 uses a width-based selection to identify CNCs in a lateral bundle of parallel particles. Such cases display either transverse "step-like" features in the object contour or gradual width changes along the major axis. SMART overlays each object with its convex hull, partitioning the hull into the object and the remaining "pockets", as shown in Fig. S5. An isolated CNC has multiple small or "flat" pockets while parallel CNC bundles show "thick" pockets with step-like features. This feature is well-captured in a geometrical measure called minimum Feret diameter, which is the distance between the two closest parallel lines restricting the object. To detect steps, objects were scanned to have a pocket with a minimum Feret diameter exceeding ~ 5 nm. Although AFM tip dilation skews width measurements, relative width changes are used to evaluate uniformity along the length and not for particle width assessment.

Step 4 utilized a height-based selection to detect vertically stacked crystals, which show sharp height variation along their major axis. SMART uses a tandem approach of chord length analysis and height profile extraction, as described in Yucel et al. (2021). SMART first aligns the CNC's major axis with the x-axis and identifies the longest horizontal chords. Then, height values of these chords are averaged perpendicular to the major axis to obtain a height profile along the length of the particle (Fig. S6a). This profile (Fig. S6b) is convolved with a 1D filter (Fig. S6b-insert) similar to a finite sign function. To identify a step, the resulting convolved profile is scanned for values exceeding 1/3 of the range of height values (Fig. S6c), excluding those near the two ends of the crystal. This threshold was chosen as a practical criterion for identifying a step and facilitating consistent identification within the scope of this analysis rather than being a natural, inherent constraint of the CNC particles. Importantly, SMART may extract and report the size characteristic of interest (solidity, bounding box, length and height) from each of the particles grouped in steps 2, 3 and 4. This study, however, focuses on reporting the dimensional measurement (length, height, height aspect ratio) of individual CNCs only.

Particle measurement

SMART measures the length, height, and the length/height aspect ratio (henceforth noted as simply aspect ratio) for each identified isolated CNC. The length is defined as the longest horizontal chord after the segmented mask of the object has been rotated so that its major axis aligns with the x-axis. AFM tip deconvolution approaches were not applied, as it was assumed that the artificial increase in length from AFM tip convolution effects was a small fraction of the total length. Note that the ILC results confirm this assumption as the consensus values for TEM and AFM length derived from 10 data sets for each method were 94.5 nm and 95.8 nm, respectively (Bushell et al 2021). For height measurement, the segmented image is used to locate the pixels inside the bounded CNC area and the height value at each pixel is extracted from the corresponding original as-received image file. The height is then calculated as the average of the tallest 20% of the height values (Fig. S7). This approach deviates from manual analysis, which determines a particle height as the difference between the maximum height along a line drawn through the major axis of an object and the background height based on the localized values at the ends of the object. The parameter for averaging the top region that is used in SMART was determined empirically through comparisons between the 2D height profiles of SMART and the 1D height profiles of manual analysis for several CNCs to provide higher consistency between height measurements and minimize the influence of any outlier height data. The aspect ratio is calculated by dividing the measured length by the measured height.

[1] The ratio of the major axis to the minor axis dimensions.

[2] Object area divided by the convex area (the area of the convex hull surrounding the object).

Table 2 Test sets for the complete and 5-image dataset studies

	Complete Dataset Study				5-Image Dataset Study				
	Lab2	Lab6	Lab7	Lab10	Lab2-5	Lab2-5-RF	Lab6-5	Lab7-5	Lab10-5
Number of images	40	25	47	44	5	5	5	5	5

RF Re-flattened images

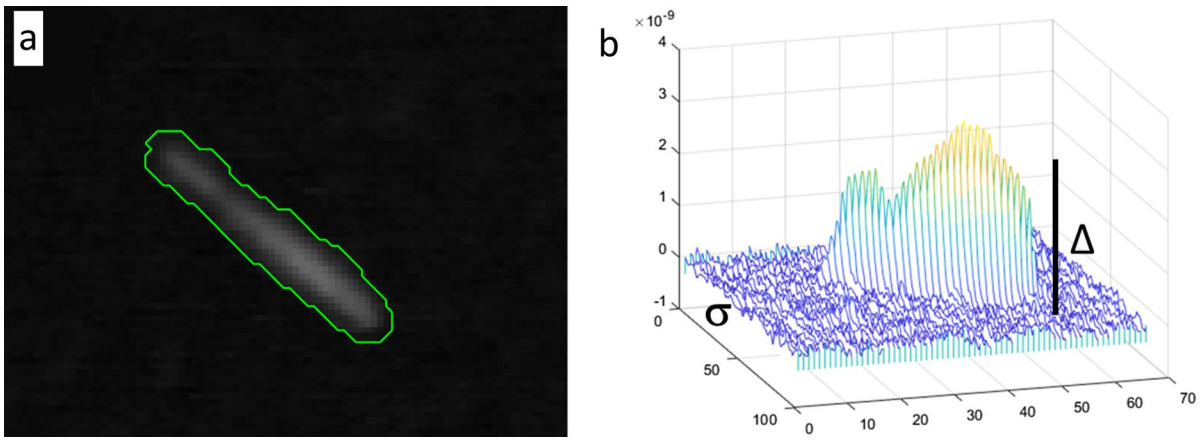

Fig. 2 SMART analysis of AFM image quality. **a** 8-bit image from Lab2 with SMART identified periphery, **b** 3D image, showing background noise (σ) which is the standard deviation of the height values for pixels segmented as background, and the contrast (Δ) which is the difference between the average height value for pixels segmented as CNC particles and the average height value for pixels segmented as background

SMART test sets

The analysis test sets used in this study are summarized in Table 2. These include either the complete image dataset, or a subset of 5 randomly selected images captured with a single AFM tip from a laboratory. Full datasets are used for statistical analysis, while the 5-image subsets evaluate the image processing, particle identification, and measurement performance of SMART as well as the impact of AFM image flattening, and particle-by-particle comparisons with manual analysis.

Image quality assessment

AFM image quality affects CNC identification and measurement, necessitating quantified metrics for evaluation. Variation in image quality between laboratories can arise from differences in instruments, probes, and probe wear. Image quality is assessed based on three factors: background noise, contrast, and CNC distribution density on the substrate. As depicted in Fig. 2, background noise (σ) is the standard deviation of height for pixels in the segmented background, while contrast (Δ) is the difference between the average height of the foreground (CNCs) and the background (substrate). To calculate background noise and contrast, SMART uses the segmented masks to identify background pixels, then averages pixel intensities in the as-received image. CNC distribution density is calculated as the ratio of total CNC area to total image area and can be further categorized into each of the individual, agglomerated, and border CNC groupings. These three image quality metrics are calculated for each image and averaged across the dataset for each laboratory. These metrics provide an unbiased assessment of errors affecting SMART's CNC identification and measurement ability.

Skew normal distributions

Despite standardized sample preparation and AFM imaging protocols, variations in identified CNCs and variability in the measured particle size distributions made direct comparisons between different datasets challenging. To this end, measurements were modeled as a skew normal distribution, providing a

Table 3 SMART assessed image parameters for each laboratory (Complete Dataset)

	Lab2	Lab6	Lab7	Lab10
Background Noise (nm)	0.4–1.0	0.3–0.8	0.4–1.0	0.4–1.4
Contrast (nm)	2.1–3.0	2.0–3.0	2.2–3.0	2.5–3.5
CNC distribution density (%) *	8.9–17.1	4.6–14.3	8.8–18.1	6.8–17.6
Isolated CNC % of total image area	0.5–3.2	0.3–3.0	0.4–2.9	0.5–2.2
Aggregate CNC % of total image area	5.4–12.9	2.5–7.5	4.4–11.2	2.1–8.5
Border CNC % of total image area	0.9–6.0	0.6–5.8	1.9–6.8	1.0–8.4

*CNC distribution density is the ratio of total CNC area to the total image area, given as a percentage

unified statistical description to compare data across laboratories and methods while accounting for a skewed asymmetry in data. Treating CNC measurements as a random variable, the distribution of length, height and aspect ratio were fit to a skew normal probability density function (PDF) (Meija et al. 2020; Bushell et al. 2021):

$$PDF(x,\alpha,\xi,\omega) = \frac{2}{\omega\sqrt{2\pi}} e^{-\frac{(x-\xi)^2}{2\omega^2}} \int_{-\infty}^{\alpha\left(\frac{x-\xi}{\omega}\right)} \frac{1}{\sqrt{2\pi}} e^{-\frac{t^2}{2}} dt$$

where x is a continuous random variable, α is the shape, ξ is the location, and ω is the scale. Fit parameters were obtained by minimizing the negative log-likelihood function for each measurement dataset, using the Python Scipy Skewnorm library.

Results and discussion

This study used SMART-AFM to analyze AFM images from four laboratories participating in an ILC study (Bushell et al. 2021) on AFM imaging and image analysis protocols for CNC particle size distributions. The images were of high quality with low background noise, strong CNC-background contrast, distinct CNC edges, and a relatively low CNC dispersion density that minimizes agglomeration—critical factors for both manual and SMART image analyses. Representative AFM images from laboratories are shown in Fig. S8. SMART was evaluated against the conventional manual approach of the ILC study using two dataset studies: a 5-image subset study (LabX-5) and a complete dataset study (LabX). The 5-image study guided SMART parameter selection by comparing SMART and manual analysis in: object identification, CNC size measurement, and AFM artifact assessment. The complete dataset study investigated image quality, consistency, SMART versus manual performance, and representative measurement assessment. All analyses were conducted in MATLAB Online.

Image quality assessment

Low-quality AFM images can compromise CNC identification and measurement for both SMART and manual methods, making image assessment essential before analysis. Images with high background noise and/or low contrast can cause substrate pixels to be mistakenly attached to adjacent objects, leading to rough, pixelated CNC boundaries that affect the performance of SMART. Table 3 and Fig. 3 summarize image quality metrics across all datasets. Background noise (0.5–0.8 nm), contrast (2.5–3.1 nm), and CNC dispersion density (4–18%) were consistent across laboratories, confirming that ILC imaging protocols effectively minimized sample and imaging variability. Individual CNCs comprised 10–50% of all CNC objects in an image, independent of CNC dispersion densities (Fig. S9a). The consistency and successful SMART analysis across datasets demonstrate that image quality remained above the critical threshold for a reliable SMART analysis, based on the three metrics in Table 3.

Identification comparison

The 5-image dataset study compared CNC identifications by SMART to the manual identification from the ILC study (Bushell et al. 2021). All SMART- and manual-identified individual CNCs were visually inspected and labeled either as a (a) Shared identifications—a CNC object identified by both approaches, (b) Unshared identification—a CNC correctly identified only by one approach or (c) Misidentification—a non-individual CNC mistakenly identified as a CNC.

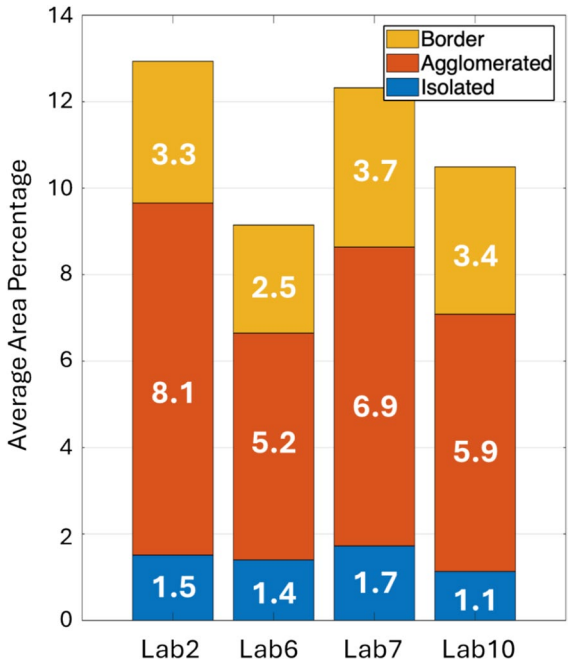

Fig. 3 Average area fractions of each CNC group (i.e., isolated, agglomerated, and border) over total image area for each laboratory. Complete dataset study

All the shared and unshared objects were considered correct individual CNC identifications by the given approach, while misidentifications are considered incorrect. Our classification was conservative, assuming idealized CNC morphology with minimal stepwise features in width or height, aligning with SMART's selection criteria. However, this process remains subjective, and thus our assessments should be considered as qualitative. Figure 4 shows the identified CNC counts in each group for both SMART (SM) and manual (MN) analysis for image sets Lab2-5, Lab6-5-Tip1, Lab7-5, Lab10-5. (The remaining Lab2-5-RF, Lab6-5-Tip2 test sets in Fig. 4 are discussed in a later sub-section—AFM Imaging Artifact Assessment).

Across the four datasets (Lab2-5, Lab6-5-Tip1, Lab7-5, Lab10-5), a total of 20 images were analyzed, with SMART and manual identifying 239 and 241 CNCs, respectively. Of these, 154 CNCs (64% of total identifications by either approach) were shared, demonstrating a considerable agreement. In addition, SMART and manual identified 51 and 59 additional unshared, but correct identifications, respectively, while misidentifications totaled 34 (SMART) and 28 (manual). Identification accuracy, defined as correct identifications relative to total identifications, was similar for both

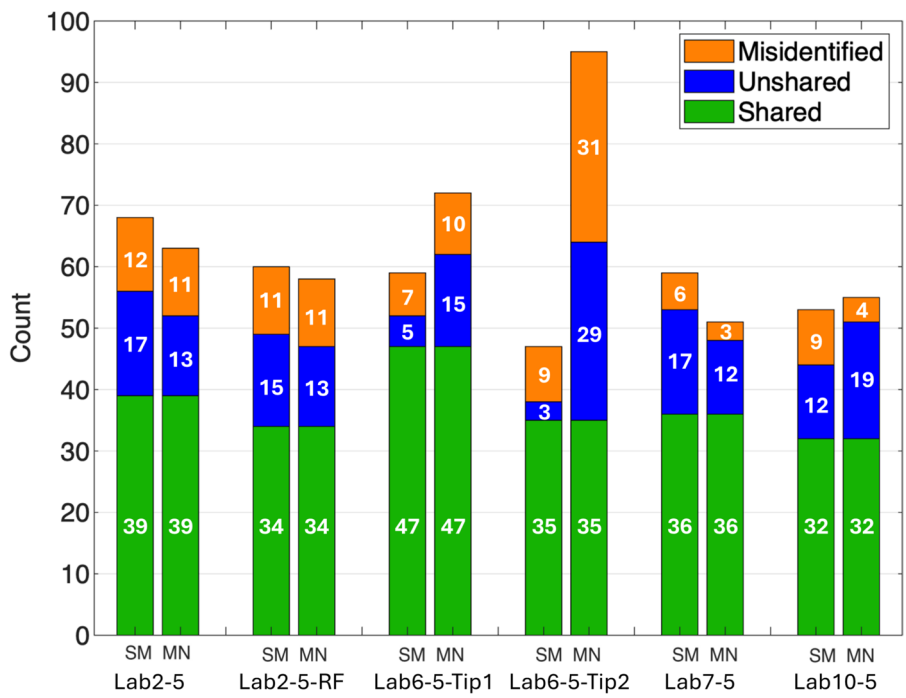

Fig. 4 Comparison of SMART and manual analysis for CNC identification from the 5-image dataset study: Misidentified (incorrect identification), unshared identification (correctly identified by one method but not the other), and shared identification (correctly identified by both methods); SM = SMART, MN = manual

approaches—86% for SMART and 88% for manual. Across laboratories, accuracy ranged 82–90% (SMART) and 83–94% (manual). All samples were produced and imaged using a similar procedure resulting in images with similar background noise, contrast, and CNC density (Table 3), therefore, the variability across laboratories may stem from imaging artifacts and analysis bias. Manual bias arise from analyst subjectivity and SMART bias is from the predefined selection criteria applied uniformly to all images.

Unshared CNCs account for 21% (SMART) and 24% (manual) of the total identifications. The manual unshared CNCs (i.e., not identified by SMART but correct) were primarily short (less than 30 nm), low contrast CNCs, insufficiently separated from other CNCs, leading to segmentation errors (Fig. S10), or were negatively impacted by imaging artifacts (see subsection AFM Imaging Artifact Assessment).

The misidentification fraction can be used to assess the reliability of the approach—the lower this fraction, generally the more accurate the analysis is expected to be. Misidentifications ranged 12–18% (SMART) and 6–17% (manual) across laboratories. SMART misidentifications resulted from either partial crystal detached from agglomerates (Fig. S11), or slight deviations from "idealized" CNC geometry (Fig. S12a). Manual misidentifications were primarily due to slight deviations from the "idealized" CNC geometry (Fig. S12b), or difficulty distinguishing individual CNCs close to a cluster.

There is a subtle variation in the philosophy of CNC detection between manual and SMART analyses. The manual method is robust and flexible, but subjective, relying on the interpretations of the analyst for acceptable CNC morphology and varying criteria for CNC grouping (e.g., using a different approach for features that are identified by SMART as vertically stacked agglomerates). SMART applies uniform selection criteria but conservatively assumes CNCs follow a singular, idealized shape. The scientific community has yet to establish a consensus on defining an acceptable level of deviation from the "idealized" CNC geometry.

CNC size measurement comparison

For mutually identified isolated CNCs (see Identification Comparison), SMART and manual CNC length measurements were generally consistent, with SMART measurements typically shorter but within 10% of the manual values (Fig. S13). The magnitude of difference correlated with CNC length, and the mean squared error (MSE) between SMART and manual length measurements was 8.9, 9.1, 8.7 and 8.4 nm for Lab2-5, Lab6-5, Lab7-5 and Lab10-5, respectively. The shorter SMART length measurement is due to the lower contrast at the tapering ends of CNC objects (CNCs exhibit spindle morphology), leading to segmentation-based trimming of the CNC ends. In some outliers (e.g., Object i in Fig. S13), height variations within the CNC led to SMART trimming the particle from the middle, significantly underestimating CNC length. SMART CNC height measurements closely matched manual results, with an average difference of 4.2% and MSE values of 0.47, 0.23, 0.22, and 0.35 nm for Lab2-5, Lab6-5, Lab7-5 and Lab10-5, respectively. The largest height measurement deviation occurred in Lab2, and can be attributed to inadequate AFM image flattening, which causes issues for SMART analysis. The overall agreement in height measurements demonstrates the consistency between SMART and manual approaches.

AFM imaging artifact assessment

The effectiveness of SMART is negatively impacted by imaging artifacts that were aligned to the scanning direction, such as, abnormally tall height spikes, wide dark background areas adjacent to CNCs that are indicative of problems with flattening, narrow bright bands on some scan lines, and uneven edges of particles. While SMART can identify and correct height spikes (Fig. S1b and c), during AFM image pre-processing, other artifacts must be manually addressed before analysis. Pre-screening for imaging artifacts before SMART analysis is recommended, either by correcting or removing affected images. The effect of flattening issues, narrow banding and uneven particle edges on SMART analysis were further investigated.

The dark background areas (10–100 pixels wide) in Lab2 images are typical features of inadequate AFM image flattening due to a failure to mask CNC particles (Figs. S8a and S14a). These bands skewed pixel

intensities, leading to issues in capturing the CNC boundary, and consequent erroneous CNC grouping and/or measurement. The hypothesis that these effects were due to flattening was confirmed by having, the Lab2-5 images re-flattened (RF) by an analyst from Lab2 after masking CNCs in Gwyddion (Fig. S14b). This created the Lab2-5-RF test set which was analyzed by SMART and manual approaches. While re-flattening had a minor effect on CNC identification (Fig. 4), it significantly reduced SMART-manual CNC measurement differences to within ± 5% (Fig. S15). MSE for length measurements decreased from 10.22 to 3.44 nm upon re-flattening, as CNC end trimming is less pronounced after flattening (Fig. S16). For height values, MSE decreased from 0.47 to 0.31 nm, attributed to improved background height estimation (Fig. S17).

Several of the Lab6 images exhibited bright narrow horizontal bands (2–4 pixels) extending beyond individual CNCs (Fig. S18). Additionally, several images exhibited horizontal shifts in the AFM scan direction resulting in uneven zigzag edges along the long axes of the CNC particles (Fig. S19). The narrow bright lines may be indicative of improper settings for the feedback setpoint and gains for the specific tip used for the images that showed this issue. The uneven particles edges are consistent with movement of the particles during imaging, indicating that the imaging force is stronger than the interaction between CNCs and the PLL-coated mica. Since this artifact was only observed in some Lab6 images we suspect that it is related to applying higher force during imaging with some tips due to incorrect setpoint or gain settings. The problem did not appear in images from other labs, suggesting that the procedure for immobilizing CNCs on a PLL coated substrate was adequate as long as the applied force was minimized. Evidence of tip contamination (Fig. S18) is detected occasionally and may contribute to some of the issues. AFM parachuting is another possible artifact that can lead to uneven particle edges but since this is typically observed with fast scan rates, we doubt that it is the source of most of the artifacts observed for Lab6.

A 5-image study was used to assess the effect of these two imaging artifacts on CNC identification and measurement, by comparing images from an artifact-free tip (Lab6-5-Tip1) to those with artifacts (Lab6-5-Tip2), as shown in Fig. 4. These artifacts triggered the clustering selection criteria (Fig. 1) thus excluding the affected objects from further analysis. In contrast, the manual analyst recognized these distortions as artifacts and continued identifying affected objects as individual CNCs. Consequently, SMART and manual analyses considered notably different sets of CNC particles, contributing to discrepancies between SMART and manual measurements. The effect of AFM tip on SMART and manual length/height measurements was assessed. For shared CNCs only, the differences between SMART and manual measurements were minimal (Fig. S20). MSE values for Lab6-5-Tip1 (length: 9.06 nm, height: 0.23 nm) were slightly higher than for Lab6-5-Tip2 (length: 6.20 nm, height: 0.2 nm). However, when comparing shared CNCs to all identified CNCs (i.e., shared, unshared and misidentified) in Lab6-5-Tip1 and Lab6-5-Tip2 image sets (Table S6), larger differences were observed as summarized in the supplemental document. Images with artifacts (Lab6-5-Tip2) showed greater differences between SMART and manual measurements compared to artifact-free images (Lab6-5-Tip1), likely due to a large number of CNCs identified in the manual analysis of Lab6-5-Tip2 being uncommon to SMART analysis, whereas Lab6-5-Tip1 had greater overlap of identified CNCs.

Comparing laboratories with SMART

The complete image dataset for each laboratory was analyzed with SMART to assess differences between laboratories. Histogram plots for the distribution of SMART length, height and aspect ratio from the complete dataset study are given in Fig. 5 with statistical descriptions tabulated in Table 4. Skew normal distributions were fitted to the entire datasets, with fit parameters shown in Fig. 5 and listed in Table S7. These fit parameters can be transformed to calculate mean and standard deviation values, matching those in Bushell et al. (2021) (see Table S8). Measurements were further visualized as 2D histograms (Fig. S21).

The histograms, PDFs, and the mean values—length ($\overline{L}$ = 73–85 nm), height ($\overline{H}$ = 2.8–3.7 nm), and aspect ratio ($\overline{AR}$ = 21–30) were similar between laboratories. The PDF fits provide a continuous representation of the data enabling the overlapped area between laboratory pairs (denoted as overlap index) to quantify the similarities between distributions (Fig. 6). For length measurements, the overlap index for all pairs of laboratories was at least

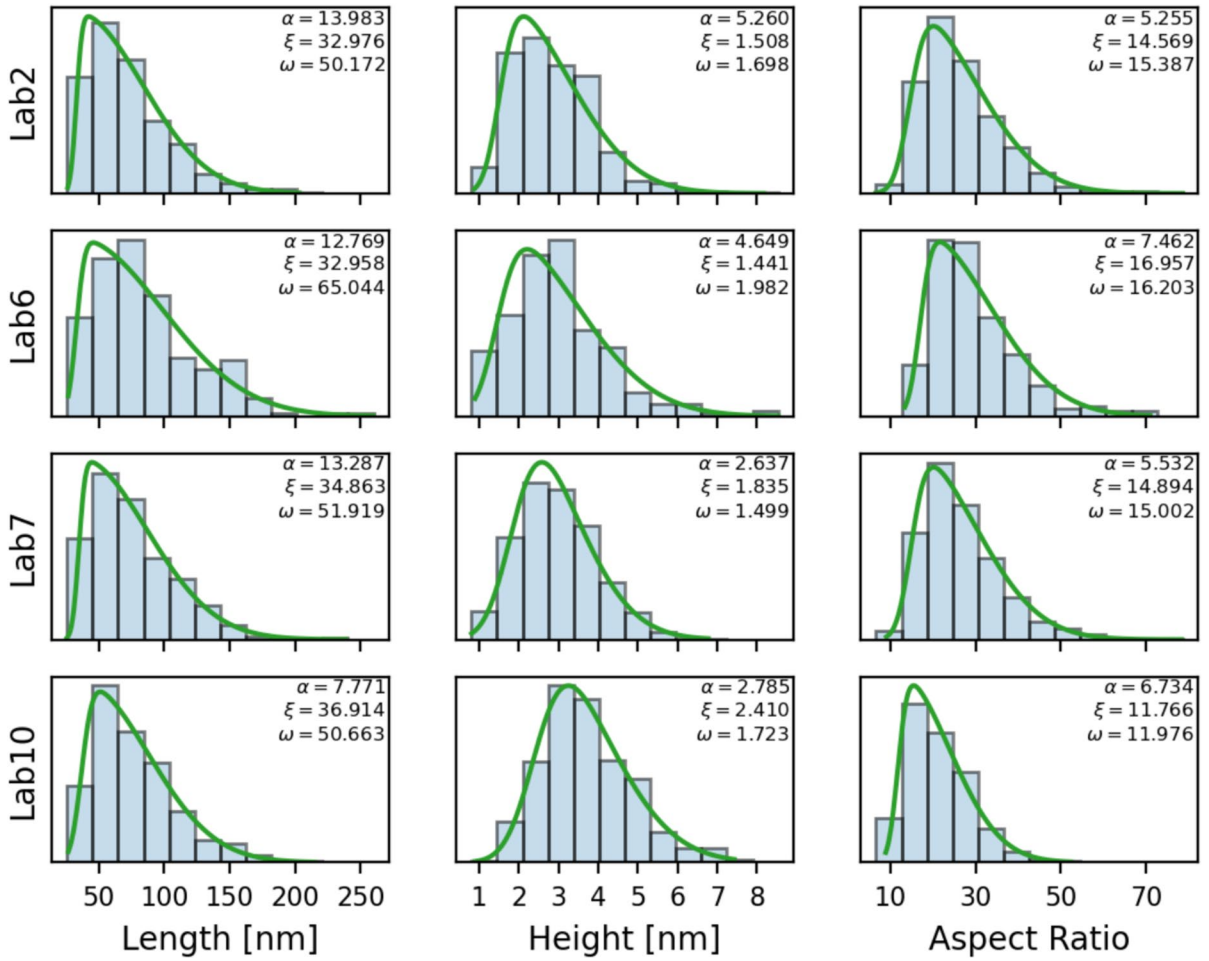

Fig. 5 Histogram plots for SMART length and height measurements and corresponding aspect ratios for each lab with skew normal distributions overlaid in green and the corresponding fitting parameters shown (α, ε, ω). Complete dataset study. Bin width was 19.5 nm for length, 0.64 nm for width, and 6 for aspect ratio

Table 4 SMART versus manual analysis summary for each laboratory. (Complete dataset)

	Lab2		Lab6		Lab7		Lab10	
	SMART	Manual	SMART	Manual	SMART	Manual	SMART	Manual
# CNCs	551	544	240	409	702	620	471	500
# CNC per image	13.8	13.6	9.6	16.4	14.9	13.2	10.7	11.4
$\overline{L}$ (σ) nm	73 (30)	83 (31)	85 (39)	99 (42)	76 (31)	79 (30)	77 (31)	82 (34)
$\overline{H}$ (σ) nm	2.8 (1.1)	2.9 (0.8)	3.0 (1.2)	3.3 (1.3)	3.0 (1.0)	3.1 (1.2)	3.7 (1.1)	3.5 (1.2)
$\overline{AR}$	27 (10)	31 (13)	30 (10)	32 (12)	27 (9)	28 (9)	21 (7)	24 (9)
Total Time (mins)	6.6**	272 *	2.9**	205*	8.6**	310*	5.9**	250*

Mean length ($\overline{L}$), height ($\overline{H}$), and aspect ratio ($\overline{AR}$) with standard deviation in brackets. Computed using skew normal distribution parameters.

*Estimated manual analysis time based on 30 s per CNC.

**SMART analysis time does not include time to optimize pre-processing parameters.

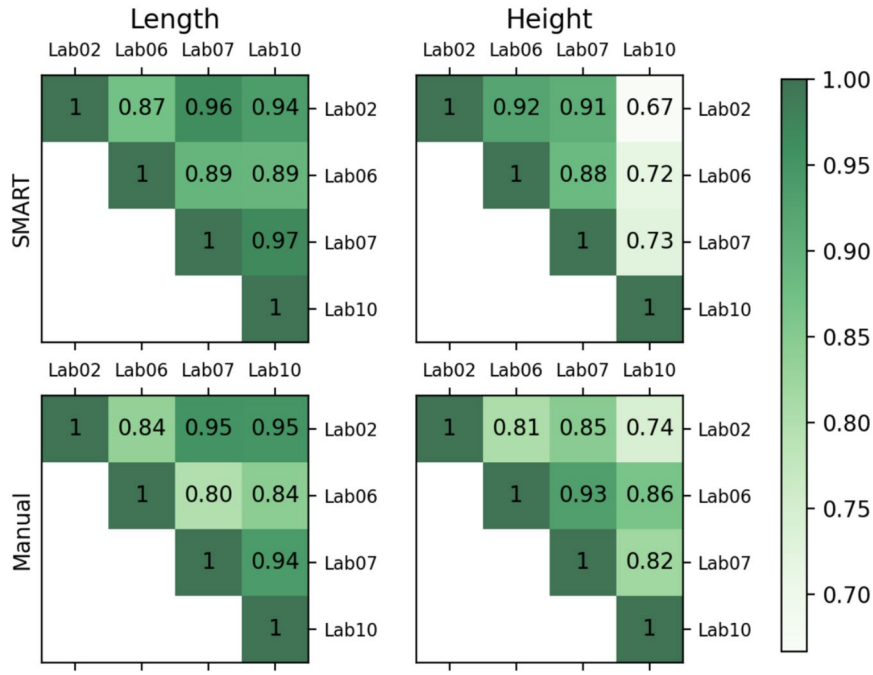

Fig. 6 Area of overlap (overlap index) between skew normal PDF fits for length and height measurements for each laboratory. Complete dataset study. The top row are the overlap indices using SMART and the bottom row are those for the manual method (similar to figure 6 within Bushell et al. (2021), for comparison, but recalculated using the skew normal fit parameters for this study)

87%, indicating strong similarity across laboratories. For height measurements, Lab2, Lab6, and Lab7 showed similar overlap index, while Lab10 had a lower index (less than 73%) as its CNC height measurements were consistently larger than those from other laboratories. Overall, this demonstrates a consistency in CNC measurements using SMART for the four laboratories.

Since SMART image analysis was applied consistently across laboratories, any variability would likely stem from inconsistencies in image quality differences or imaging artifacts. However, the small variation between laboratories indicates that differences in background noise, contrast, and CNC distribution density (Table 3) were not substantial enough to influence CNC identification and measurement. Interestingly, while Lab2 (inadequate image flatting) and Lab6 (AFM tip effects) exhibited observable imaging artifacts in the 5-image dataset study, these effects did not lead to notable discrepancies in the complete dataset measurement results. This suggests that differences observed in the smaller dataset (tens of objects) were averaged out with increased CNC measurements to hundreds of objects in the full dataset.

SMART versus manual analysis

To evaluate the accuracy of SMART, the analysis results are compared with those of the manual approach. Individual CNC identification counts were similar for Lab2, Lab7, and Lab10, but substantially lower for Lab6 using SMART where AFM tip-induced imaging artifacts resulted in the exclusion of many affected objects. In contrast, manual analysis was more tolerant of objects with altered morphologies due to these artifacts. SMART analysis runtime ranged 3–8 min per laboratory. Although manual analysis time was not explicitly reported, an estimated 30 s per CNC was used, accounting for isolated CNC identification, measurement (involving drawing lines over the CNCs), and data recording. Based on this, manual analysis was estimated to take 200–310 min per laboratory.

Overall, SMART and manual methods showed strong agreement (Table 4, Fig. S21) with the dominant disparity being that SMART length measurements were 7.3–16.5% lower, attributed to segmentation-based trimming of CNC ends. Despite this, both methods produced similar skew normal PDF fits and high overlap indices across laboratories (Fig. 7). All skew normal distribution fits (length, height and

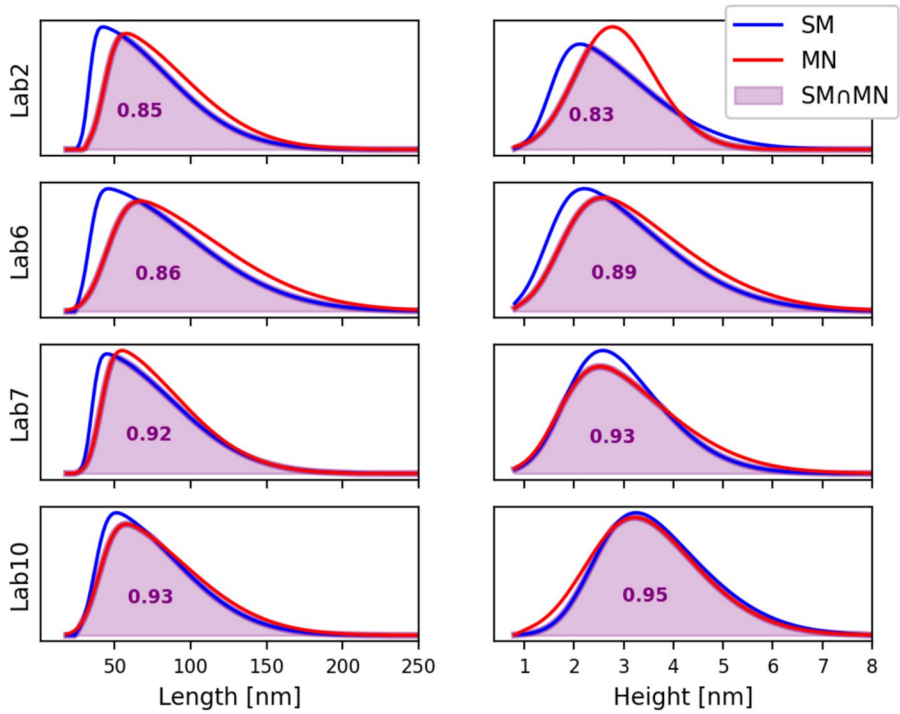

Fig. 7 Skew normal PDF fits for length and height measurements for SMART and Manual methods for each laboratory. Overlap regions are shaded and labeled with the corresponding overlap index. Complete dataset study

aspect ratio for both SMART and manual) show a right skew with a peak shifted toward lower values. The length distributions from SMART were slightly shifted to shorter lengths compared to manually measured CNCs. SMART-manual overlap indices for length and height were similar across laboratories, with higher values for Lab7 and Lab10 than for Lab2 and Lab6, likely due to the presence of imaging artifacts in Lab2 (inadequate flattening) and Lab6 (AFM tip artifact). Inter-laboratory comparison indicated that length measurement variation was lower for SMART (87–97% overlap) than for manual (80–95%), suggesting SMART provides more consistent length measurement across laboratories (Fig. 6). As for height, Lab2, Lab6, and Lab7 showed high overlap index, while CNC height values for Lab10 were higher which resulted in a lower overlap index (71–73%) with other laboratories. Since SMART and manual produced similar height distributions for Lab10 (95% overlap), the height difference potentially reflects a real sample feature of Lab10 rather than an analysis issue, further supported by the closeness of Lab10 manual height measurements to the consensus values for height reported in the ILC study (Bushell et al. 2021).

The differences between SMART and manual analyses were comparable to the variability observed between two analysts in the CNC reference material characterization (Jakubek et al. 2018). The initial phase of the ILC study also tested the manual image analysis protocol on a single image set and indicated slightly lower variability across participants. These findings confirm that SMART achieves similar accuracy to manual analysis while being significantly faster and applying a more consistent, standardized selection criteria across laboratories.

Representative measurement assessment

Determining the number of CNC measurements required to ensure a representative measurement with an acceptable uncertainty involves assessing when the cumulative average stabilizes within a specified deviation (e.g., 5–10%). SMART facilitates this assessment by analyzing two parameters: variation in the cumulative average as additional images are analyzed, and acceptable deviation thresholds. SMART calculates cumulative means of length and height as additional AFM images are analyzed, based on arithmetic means rather than skew normal distributions. By tracking these changes with additional images, a

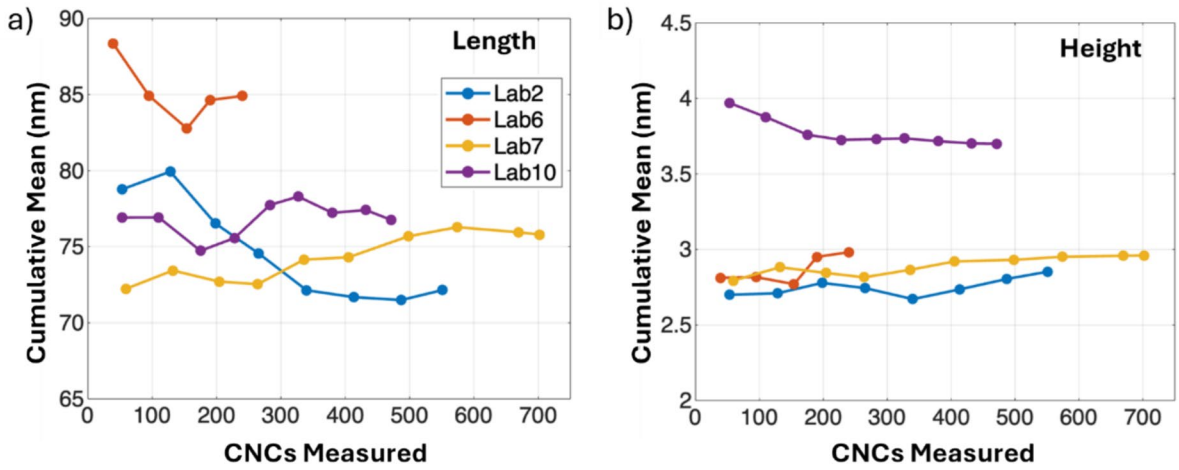

Fig. 8 Change in the cumulative mean with each analysis of an additional grouping of 5 images. **a** Cumulative mean length. **b** Cumulative mean height. For each laboratory the cumulative means (length and height) appear to stabilize, having a deviation of less than 5–10% between the last 3–4 image analysis groupings, suggesting that a representative measurement has been achieved

stable representative measurement, and a reasonable estimate is indicated when the variation between successive groupings of images falls below the specified deviation. Figure 8 shows the cumulative mean length and height curves from four laboratories, analyzed in batches of 5 images. Initially, the cumulative mean may oscillate but stabilize as more CNCs are analyzed, as observed for Lab2, Lab7, and Lab10 (but less so for Lab6). For the analysis of the last 3–4 batches of 5 images, the variation in cumulative means was below 5–10%, suggesting that a representative measurement had been achieved. These results align with the common practice of analyzing 300–500 CNCs to ensure a representative measurement. Additionally, SMART can be used during the imaging process to guide the analyst to determine when a sufficient number of images have been collected.

Conclusion

Reliable and rapid measurement of CNC particle dimensions (length and diameter) is crucial for quality control, grade definition and investigating morphology-performance relationships in various applications. This study proposes a semi-automated, open-source image analysis framework, SMART-AFM, that processes AFM images to segment CNCs from an imaging substrate, classifies CNCs into morphologically distinct groups and reports their dimensional measurements. An assessment of the performance of SMART-AFM on a dataset of AFM images from the ILC study (Bushell et al. 2021) is presented. This assessment, focusing on individual CNCs only, benchmarks particle identification, dimensional measurement and efficiency against the non-automated, analyst-dependent manual approach. On a 20-image test set, accurate particle identifications accounted for 86% and 88% for SMART-AFM and manual, respectively, with 64% shared identifications between the approaches. SMART-AFM consistently measured CNC length 7–17% shorter than manual approach due to segmentation-based trimming of CNC tails. SMART-AFM and manual height measurements were in close agreement, with an average difference of 4.2%. SMART-AFM exhibited greater similarity than the manual approach for CNC length measurements across laboratories, reducing analyst-dependent subjectivity and variability inherent in manual method. SMART-AFM processed the ILC image set (154 images) over 40 times faster than the estimated processing time of manual (approximately 0.16 and 6.43 min per image, respectively). This benchmarking demonstrated the reliability and efficacy of SMART-AFM as a standardized, automated workflow for CNC analysis from AFM images. SMART-AFM effectively addresses image noise reduction,

contrast adjustment and some imaging artifacts (AFM scan bright spikes). However, for optimal performance, using high-quality AFM images is recommended—low noise, strong CNC-background distinction, sufficiently low CNC distribution density on imaging substrate to prevent agglomeration and free from artifacts such as inadequate flattening and AFM tip contamination. The SMART-AFM framework includes user-adjustable parameters for image processing and particle grouping, customizable for analyzing various CNC morphologies, although a unified parameter set was applied across all laboratories in this study. SMART-AFM can support CNC research and development, such as in assessing CNC dispersion efficiency as a function of sonication energy (Johns et al. 2023, Parton et al. 2023) and measuring particle size distributions for regulatory compliance and batch-to-batch consistency. The SMART-AFM code and tutorial is available for public use for free at Github™. [https://github.com/sabbkarr/SMART-AFM/].

Acknowledgments We would like to recognize Byong Chon Park (Korea Research Institute of Standards and Science) and Lingling Ren (National Institute of Metrology, China) for providing two of the ILC data sets (AFM images, and manual image analysis). We would like to recognize Katherine Lin of National Research Council Canada for re-flattening Lab2 images and completing manual image analysis.

Author contribution The study conception was developed by R.M., S.Y., L.J. and S.Kal.. The study design was developed by R.M., S.K., and S.Y.. Coding design was developed by S.K, S.Y., and S.Kal.. Code testing and verification studies was completed by S.K. and R.M.. Skewed Normal calculations and analysis completed by N.B.. Results analysis was completed by S.K., R.M., N.B., and L.J.. ILC AFM image datasets were provided by W.B. and J-Y.C. The main manuscript text was written by R.M, and S.K.. All authors critically reviewed a draft manuscript(s), which resulted in revisions to the document. All authors have read and approved the final manuscript.

Funding This work was supported by USDA Forest Service, Forest Products laboratory (Grant Number: 18-JV-11111129-040 and 22-JV-11111129-036) and the Renewable Biomaterials Institute at Georgia Institute of Technology.

Data availability No datasets were generated or analysed during the current study.

Declarations

Conflict of interest The authors declare no competing interests.

References

Bushell M et al (2021) Particle size distributions for cellulose nanocrystals measured by atomic force microscopy: an interlaboratory comparison. Cellulose 28:1387–1403. https://doi.org/10.1007/s10570-020-03618-4

CNCD-1 (2016). National Research Council Canada. CNCD-1: Cellulose Nanocrystal Powder Certified Reference Material. https://doi.org/10.4224/crm.2016.cncd-1

da Silva LC, Cassago A, Battirola LC, Gonçalves MdC, Portugal RV (2020) Specimen preparation optimization for size and morphology characterization of nanocellulose by TEM. Cellulose 27:5435–5444. https://doi.org/10.1007/s10570-020-03116-7

Delepierre G, Vanderfeet OM, Niinivaara E, Zakani B, Cranston ED (2021) Benchmarking cellulose nanocrystals part II: new industrially produced materials. Langmuir 37:8393–8409. https://doi.org/10.1021/acs.langmuir.1c00550

Elazzouzi-Hafraoui S, Nishiyama Y, Putaux J-L, Heux L, Dubreuil F, Rochas C (2009) The shape and size distribution of crystalline nanoparticles prepared by acid hydrolysis of native cellulose. Biomacromol 9:57–65. https://doi.org/10.1021/bm700769p

Foster EJ et al (2018) Current characterization methods for cellulose nanomaterials. Chem Soc Rev 47:2609–2679. https://doi.org/10.1039/C6CS00895J

Grachev V, Deschaume O, Lang PR, Lettinga MP, Bartic C, Thielemans W (2024) Dimensions of cellulose nanocrystals from cotton and bacterial cellulose: comparison of microscopy and scattering techniques. Nanomaterials 14:455. https://doi.org/10.3390/nano14050455

Hotaling NA, Bharti K, Kriel H, Simon CG Jr (2015) DiameterJ: a validated open source nanofiber diameter measurement tool. Biomaterials 61:327–338. https://doi.org/10.1016/j.biomaterials.2015.05.015

Jakubek ZJ et al (2018) Characterization challenges for a cellulose nanocrystal reference material: dispersion and particle size distributions. J Nanopart Res 20:98. https://doi.org/10.1007/s11051-018-4194-6

Johns MA, Lam C, Zakani B, Melo L, Grant ER, Cranston ED (2023) Comparison of cellulose nanocrystal dispersion in aqueous suspension via new and established analytical techniques. Cellulose 30:8259–8274. https://doi.org/10.1007/s10570-023-05348-9

Johnston LJ (2024) Cellulose nanomaterial metrology: microscopy measurements. Nanoscale 16(40):18767–18787. https://doi.org/10.1039/d4nr02276a

MATLAB (2020) version R2020a. The MathWorks Inc. https://www.mathworks.com/help/images/ref/imclearborder.html?s_tid=doc_ta, https://www.mathworks.com/help/images/ref/regionprops.html

Mattos BD, Tardy BL, Rojas OJ (2019) Accounting for substrate interactions in the measurement of the dimensions of cellulose nanofibrils. Biomacromol 20(7):2657–2665. https://doi.org/10.1021/acs.biomac.9b00432

Meija J et al (2020) Particle size distributions for cellulose nanocrystals measured by transmission electron microscopy: an interlaboratory comparison. Anal Chem

92:13434–13442. https://doi.org/10.1021/acs.analchem.0c02805

Moon RJ, Martini A, Nairn J, Simonsen J, Youngblood J (2011) Cellulose nanomaterials review: structure, properties and nanocomposites. Chem Soc Rev 40(7):3941–3994. https://doi.org/10.1039/C0CS00108B

Parton TG, Parker RM, Van De Kerkhof GT, Narkevicius A, Haataja JS, Frka-Petesic B, Vignolini S (2023) Chiral self-assembly of cellulose nanocrystals is driven by crystallite bundles. Nature Commun 13:2657. https://doi.org/10.1038/s41467-022-30226-6

Persson NE et al (2017) High-throughput image analysis of fibrillar materials: a case study on polymer nanofiber packing, alignment, and defects in organic field effect transistors. ACS Appl Mater Interfaces 9(41):36090–36102. https://doi.org/10.1021/acsami.7b10510

Reid MS, Villalobos M, Cranston ED (2017) Benchmarking cellulose nanocrystals: from the laboratory to industrial production. Langmuir 33(7):1583–1598. https://doi.org/10.1021/acs.langmuir.6b03765

Schütz C, Rie JV, Eyley S, Gencer A, Gorp HV, Rosenfeldt S, Kang K, Thielemans W (2018) Effect of source on the properties and behavior of cellulose nanocrystal suspensions. ACS Sustain Chem Eng 6:8317–8324. https://doi.org/10.1021/acssuschemeng.8b00334

Sokolov P, Belousov M, Bondarev SA, Zhouravleva GA, Kasyanenko N (2017) FibrilJ: ImageJ plugin for fibrils' diameter and persistence length determination. Comput Phys Commun 214:199–206. https://doi.org/10.1016/j.cpc.2017.01.011

Usov I, Mezzenga R (2015) Fiberapp: an open-source software for tracking and analyzing polymers, filaments, biomacromolecules, and fibrous objects. Macromolecules 48(5):1269–1280. https://doi.org/10.1021/ma502264c

Wang X et al (2021) Autodetect-mNP: an unsupervised machine learning algorithm for automated analysis of transmission electron microscope images of metal nanoparticles. JACS Au 1:316–327. https://doi.org/10.1021/jacsau.0c00030

Willhammar T et al (2021) Local crystallinity in twisted cellulose nanofibers. ACS Nano 15(2):2730–2737. https://doi.org/10.1021/acsnano.0c08295

Yucel S, Moon RJ, Johnston LJ, Yucel B, Kalidindi SR (2021) Semi-automatic image analysis of particle morphology of cellulose nanocrystals. Cellulose 28:2183–2201. https://doi.org/10.1007/s10570-020-03668-8

Yucel S, Moon RJ, Johnston LJ, Fox DM, Park BC, Foster EJ, Kalidindi SR (2022) Transmission electron microscopy image analysis effects on cellulose nanocrystal particle size measurements. Cellulose 29:9035–9053. https://doi.org/10.1007/s10570-022-04818-w